Elastic Scattering of Low-Energy Pions and Muons from Lead*

G. Dugan, S. Childress, L. M. Lederman, L. E. Price, and T. Sanford†
Columbia University, New York, N.Y.
(Received 23 February 1973)

The small-angle (13°–40°) part of the elastic differential cross section for the scattering of low-energy ($T_\pi \sim 100$ MeV) positive and negative pions from natural lead was measured. The same quantity was also measured for the scattering of low-energy muons from lead. The muon-lead data were used to determine the rms charge radius of the lead nucleus. Assuming a Fermi shape for the charge density with a skin thickness of 2.21 fm, the result was $\langle r^2\rangle_{\rm ch}^{1/2} = 5.50 \pm 0.06$ fm. The $\pi^\pm$-Pb data, taken in the region of large Coulomb nuclear interference, were compared with predictions of the pion-nucleus optical model according to Watson and Kisslinger. Excellent fits to the data were obtained by treating the model phenomenologically; however, the best-fit optical-model parameters were not in agreement with the values computed from experimental pion-nucleon phase shifts. Since the $\pi^\pm$-Pb elastic cross sections are sensitive to the neutron density distribution, a determination of the rms neutron-matter radius could be made. Assuming a Fermi shape for the neutron-matter density, with a skin thickness of 2.21 fm, the result was $\langle r^2\rangle_{\rm n.m.}^{1/2} = 5.45^{+0.13}_{-0.25}$ fm.

I. INTRODUCTION

The experimental study of pion-nucleus elastic scattering at low incident pion kinetic energies (i.e., a few hundred MeV) has, in the past, been confined predominantly to light nuclei. The best example is the recent CERN collaboration[1] which measured π^- scattering from ^{12}C. These light-nuclei data have been extensively analyzed in terms of theoretical models; for the elastic differential cross section corresponding to pion kinetic energies of ~120 MeV (well below the Δ_{33} resonance), the Kisslinger model[2,3] has been shown to provide an excellent description up to at least the first diffraction minimum. However, there have been no experimental data available for an accurate test of the Kisslinger model in heavy nuclei. The experiment reported here presents data which provide such a test: the elastic differential cross section for the scattering of π^+ and π^- from natural lead, over the angular range from about 13 to 40°, at an incident pion kinetic energy in the laboratory of 96 MeV. In addition, there has recently been speculation[4] that measurements of pion elastic scattering in heavy nuclei can provide new information about nuclear structure: In particular, a comparison of π^+ and π^- elastic scattering from lead may yield information about the neutron distribution which is competitive in precision with that obtained by other techniques (see Fig. 1). However, since the data available from this experiment have only a limited angular range, were taken only at one pion energy, and have large statistical uncertainties in one case (the π^+ data), the accuracy of the neutron-matter rms radius determination presented here is somewhat lower than that of other methods.

We also report a measurement of the elastic differential cross section for the scattering of negative muons from natural lead in the same angular range and at the same momentum. The data are compared with the results of a phase-shift calculation of the Coulomb scattering from a static charge density, and the rms radius of the charge distribution of the lead nucleus is extracted.

II. EXPERIMENT

A. General

The experiment utilized a secondary pion beam from the Nevis synchrocyclotron. Figure 2 shows the general features of the beam transport system; Fig. 3 illustrates the experimental apparatus. The pion beam was deflected and focused by a dipole and quadrupole doublet behind the main shielding wall into the high-energy (A-hole) channel. The beam momentum was about 190 MeV/c. Upon emerging from the channel, the charged beam was again deflected and focused, by a dipole and quadrupole doublet, into the apparatus.

The main features of the apparatus (Fig. 3) were:
(a) A time-of-flight system to measure the velocity.
(b) A magnetic spectrometer, utilizing a dipole and a series of wire spark chambers on either side, to measure the incident momentum and the trajectory incident upon the target.
(c) A natural lead target (0.8348 gm/cm^2) in which the scattering event occurs.
(d) A set of large wire spark chambers to measure the scattered trajectory.

(e) A system of counters to measure the range of the scattered particle.

B. Time-of-Flight System

The useful time-of-flight measurements were made between the counters $C1$ and $C2$, and $C1$ and $C3$ (see Fig. 3). The principal use of these measurements was in particle identification: Since the incident beam was a mixture of pions, muons, and electrons in the approximate ratio 5:1:1, it was necessary to exclude, for example, all muons and electrons to measure the pion cross section. The time differences between the signals from the respective counters were converted to pulse heights and stored in 256-channel analog-to-digital converters (ADC's). The time-of-flight resolution in terms of β ($\beta \equiv v/c$) was on the order of 0.03 full width at half maximum (FWHM): This can be compared with the separation in velocity for particles of 190-MeV/c momentum: $\beta(\mu) - \beta(\pi) = 0.07$, $\beta(e) - \beta(\mu) = 0.13$.

C. Magnetic Spectrometer System

The magnetic spectrometer consisted of two sets of three wire spark chambers, with one set on either side of a Brookhaven 18H36 dipole magnet. The spark chambers were of the magnetostrictive readout type. The magnetostrictive pulses were amplified and digitized into scaler readings in a Science Accessories Corporation (SAC) scaler system. The chambers were calibrated by triggering them on particles of known position, defined by veto counters. The chambers measured the trajectory of a particle before and after it was deflected through ~30° in the dipole field. An NMR probe in the field provided a continuous monitor for the central field strength. The field was mapped in detail with a Hall probe, and the measurements were checked against a direct measurement of the line integral of the field through the magnet with a long flip coil. The knowledge of the trajectory deflection and the field enabled the momentum to be determined. The absolute uncertainty in the momentum measurement was estimated at 0.2%; the spectrometer system's resolution was 2 MeV/c (FWHM). The final set of spectrometer chambers also provided a measurement of the trajectory of a particle as it was incident upon the target (see Fig. 3).

D. Lead Target

The lead target was 0.8348 gm/cm^2 thick. It was determined by spectroscopic analysis to have less than 1% impurities (principally copper). It was assumed to have the isotopic composition of

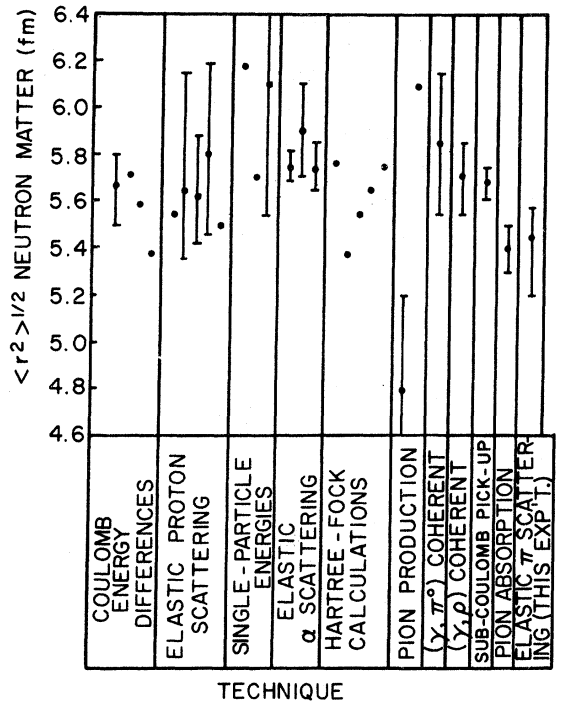

FIG. 1. Neutron-matter radius as a function of technique [see B. Tatischeff *et al.*, Phys. Rev. C 5, 234 (1972) and W. Hirt, Nucl. Phys. B9, 447 (1969)].

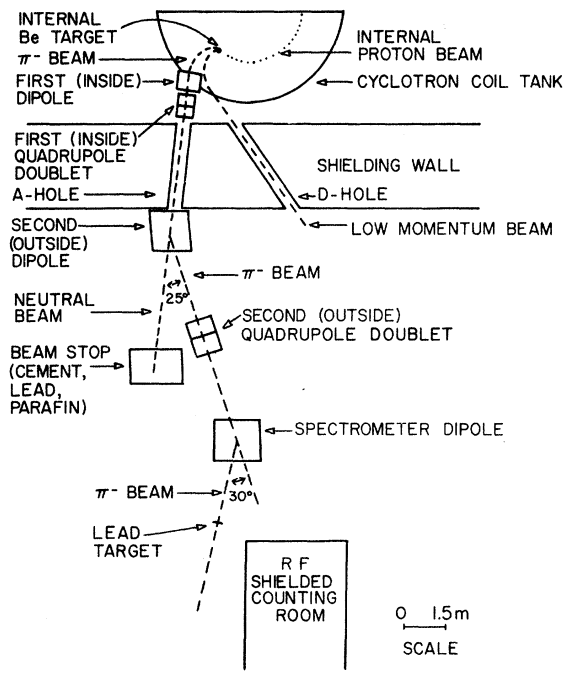

BEAM-TRANSPORT SYSTEM
(NEGATIVE BEAM)

FIG. 2. Beam transport system.

natural lead, namely, 23.6% ^{206}Pb, 22.6% ^{207}Pb, and 53.8% ^{208}Pb.

E. Scattered-Particle System

The spark chamber set after the target measured the scattering angle of events which scattered up to 40°. The chambers here were also of the magnetostrictive readout type. This set of chambers was calibrated by predicting positions of beam particles from trajectories measured in the final spectrometer set. In order to include large-angle particles in the calibration, this last set of chambers was rotated, as a unit, about a vertical axis, through known angles up to 30°, at the end of the experiment. The final result was an angle measurement with an absolute uncertainty estimated at ~0.3%. The angular resolution of the system (not including multiple Coulomb scattering in the target) was ~16 mrad (FWHM).

A valuable check on the momentum and angle calibrations was provided by the angular distribution of pion decay, with its Jacobean peak at ~210 mrad. A comparison of a Monte Carlo calculation with the results of a special data run in which the system was triggered only on pion decays implied a shift in $q \equiv p_\pi \sin\theta$ of 0.24%, which is consistent with our estimated errors in either p_π or θ.

As shown in Fig. 3, the range measurement system had the following components: (1) a lead wall of ~2.5-cm thickness, 183-cm×183-cm area, to slow the scattered particles so that they would stop in the subsequent range counters; (2) two banks of plastic scintillator hodoscope counters, each 1.3 cm thick, with a 183-cm×183-cm area; (3) six liquid scintillator range counters, each 2.5 cm thick, covering the 183-cm×183-cm area.

F. Range Measurement

The range system was arranged so that beam muons would stop in the fifth liquid range counter, on the average; and beam pions would stop in the first liquid range counter. Roughly 20% of the pion beam was absorbed in the lead wall via nuclear interactions in flight. The range resolution, determined by the thickness of the counters and the range straggling, was about 10 MeV/c (FWHM). Although the pions and muons were well separated, the range measurement was *not* used as the primary technique for π-μ-e discrimination (in order to avoid a range-efficiency correction in the analysis). The major background for the pion experiment was pion decay, as discussed below. The range measurement served to separate pion-lead scatters (signal) from about 50% of the low-energy decay muons (background) which stopped in the lead wall. However, the rest of the decay-muon background had roughly the same range as scattered pions and could not be separated by the range information. The major function of the range measurements, as used in the analysis, involved the requirement that an acceptable pion event should penetrate the lead wall and trigger at least one of the hodoscope counters. This eliminated some of the decay-muon background

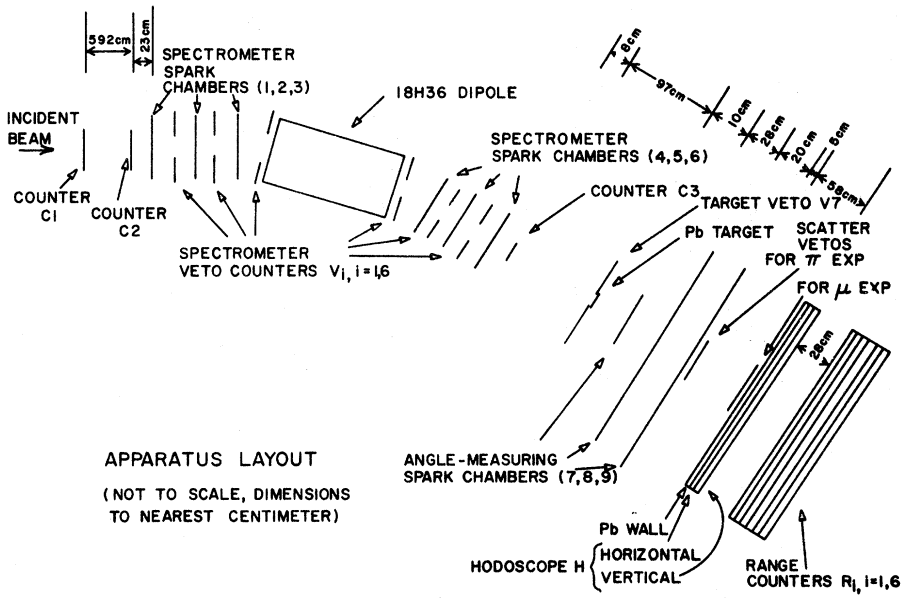

FIG. 3. Apparatus layout.

as well as most of the inelastic pion scattering in the target.

G. Logic and Procedure

The incident flux was defined as the coincidence $F \equiv C1 \cdot C2 \cdot C3 \cdot H \cdot \overline{V} \cdot \overline{V7} \cdot \overline{D}$. Here V represents all the veto counters ($V_1 \cdots V_6$) in the spectrometer system, and $V7$ represents the veto counter just before the target. D is a dead time necessary to allow the system to recover from the last event; it was ~0.1 sec. The requirement of H in the trigger implies that the particle survived the lead wall. The system was triggered on (a) "scatter" events which missed the scatter veto S, i.e., satisfied $F \cdot \overline{S}$, or (b) "beam-sample" events, which were straight-through events randomly sampled as a measure of the characteristics of the incident beam.

When an event occurred, the chambers were pulsed, and the data acquisition initiated. The chamber scaler readings, the time-of-flight ADC's, the NMR readout, and various identification bits (including bits corresponding to hodoscope and range-counter firings) were assembled in 29 32-bit words and transmitted to storage on a disk on an IBM 360/44 computer. A bank of scalers monitoring critical counter and coincidence rates was also transmitted to the computer at two-minute intervals. It was not possible for the computer to do on-line analysis; the data were stored on magnetic tapes and subsequently processed as discussed below.

Data runs with the target in were taken alternatively with target-out runs, which allowed a study of the background. Table I summarizes the collected data in terms of total numbers of events.

III. ANALYSIS

A. Reconstruction

The first phase of the data analysis involved the reconstruction of the raw data (data acquisition system output). This involved a computation of the momentum (from the spectrometer information), velocity (from the time-of-flight information), scattering angle, range, and the geometry of the event (from information supplied by the last set of chambers). Other auxiliary quantities were also computed. The most important were measures of the spark-chamber and range-system efficiencies, and reconstructed trajectories in the spectrometer dipole.

The reconstruction program processed every event which had triggered the system. Many of these, however, were not suitable for various reasons; consequently, requirements were imposed to eliminate them. A given set of requirements was applied to both the "scatter" and the "beam sample" events. The flux corresponding to the surviving scatter events was determined from the effects of the requirements on the "beam sample" events.

B. Acceptance Criteria

The principal requirements imposed on the reconstructed events were the following:

1. Spark-chamber requirements. These required that at least two out of each three chambers in each of the three sets gave an unambiguous (x and y) position for the event. Possible biases which could be present in the last set of chambers, where the "scatter" and "beam sample" distributions were quite different, were looked for but not found. The largest class of events rejected by this requirement were multiple-track events in which the chamber information was ambiguous. The loss of events through this requirement was 10–20%.

2. Velocity requirements. These required that an accepted event have a velocity characteristic of the pion (for the pion experiments) or a muon (for the muon experiment), within resolution errors. The requirements involved both the $C1C2$ and $C1C3$ time-of-flight measurements. The muon contamination in the pion experiments was ~0.1% of the flux after the velocity requirements; the pion and electron contaminations in the muon experiment were respectively ~10^{-5} and ~10^{-4} of

TABLE I. Collected data totals.

	π^- Targ in	π^- Targ out	π^+ Targ in	π^+ Targ out	μ^- Targ in	μ^- Targ out
Total flux	22 118 161	5 514 648	6 455 155	2 166 176	26 322 972	7 655 250
Flux after cuts	15 173 058	3 794 078	3 601 976	1 204 393	9 035 199	2 595 889
Total events	187 421	29 923	150 449	33 139	416 452	28 885
Total scatters	113 575	10 487	115 063	21 064	326 153	7 505
Scatters after cuts	57 716	3 277	11 103	789	89 969	296

the muon flux. The requirements for rejecting muons were less severe than those for rejecting pions and electrons because there were initially more pions than muons, and the pion-scattering cross section is larger than that of the muons. Consequently, the muon rejection entailed a loss of only 15% of the pion flux, but the pion rejection entailed a loss of 60% of the muon flux.

3. Range requirements. The only range requirement was the requirement of passage through the lead wall: This was imposed by including the hodoscope H in the flux definition, or by selecting events for which the hodoscope bits were set. For the pion experiment, corrections for angle-dependent increases in nuclear absorption loss and straggling loss in the lead wall were then necessary, as discussed below.

4. Geometrical requirements. There were two principal ones. The first was a requirement that the predicted-event position after the spectrometer dipole agree with the measured position within the resolution errors. This requirement served to eliminate momentum mismeasurements. The second was a requirement that the reconstructed scattering vertex be coincident with the target position, within the resolution errors. This served to eliminate some background events. The loss of events through the first requirement was ~8%; through the second, it was ~30% for π's, 10% for μ's.

Table I shows the amounts of flux and scatter events which survived the event requirements discussed above. Histograms of the scattering angle and momentum of the good events were the final result of the reconstruction process: These histograms were then subjected to the further analysis discussed below, with the final result being the experimental elastic differential cross section.

C. Corrections

The corrections which remained to be applied to the reconstructed angular spectrum at this stage were: (1) background subtraction, (2) geometrical efficiency and angular resolution correction, (3) correction for multiple scattering in the target, (4) corrections for the finite incident momentum spread and (for the pion experiment only) corrections related to the range requirements, and (5) corrections for inelastic processes. We shall briefly discuss each of these in turn.

The target-out runs provide a measure of the background. Study of the background spectrum revealed that, for the pion experiments, it had two components: a relatively flat distribution extending over the entire angular acceptance of the system, originating from pion scattering in the air around the lead target; and a sharply peaked distribution at the smallest angles (~200 mrad) originating from the decay $\pi \rightarrow \mu + \nu$ occurring in the vicinity of the target. About half the decay muons were of sufficiently low energy that they could stop in the lead wall; but the other half survived the wall and could not be distinguished from a real target scatter event. Thus, it was necessary to eliminate both components of the background from the target in data with a background subtraction. However, the pion-decay events will undergo multiple Coulomb scattering in the target, so that the decay background in the presence of the target is actually quite different from the background as measured experimentally with the target out. Using the Monte Carlo program mentioned above, we have been able to simulate correctly the target-out pion-decay angular distribution. The target-in pion-decay background was simulated in the same way, except that now multiple Coulomb scattering in the target was allowed. A correction was made for events which scattered at large angles in the target, and also decayed, and which were therefore real signal. The resulting Monte Carlo generated angular distribution was taken as the actual pion-decay background for the target in runs. Along with the

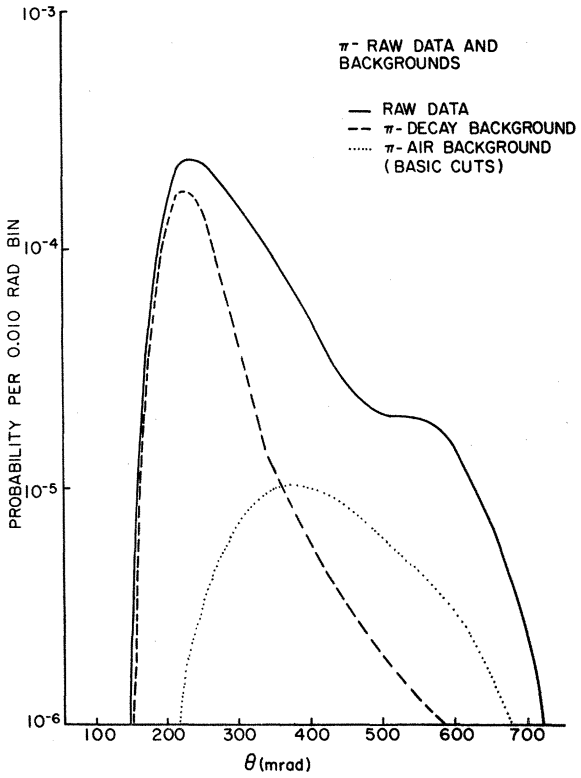

FIG. 4. π^- raw data and backgrounds.

experimental pion-air background distribution (also corrected for scattering in the target), it was subtracted from the total target in distribution to give the pion-lead scattering distribution.

A number of consistency checks were made to insure that this simulation technique was correct. The principal check involved a comparison of the final pion-lead distributions for a series of cuts on the scattering vertex location, each of which allowed a different amount of pion-decay background to be present, but did not affect events which were pion-lead scatters in the target. The consistency between the final results for the different cuts (the results differed by at most 5%) was taken as a measure of the systematic uncertainty in the background simulation technique, and is included in the errors quoted for the differential cross section. Figure 4 shows the relative sizes of the uncorrected total target in angular distribution, and the pion-decay and pion-air backgrounds, for the π^- experiment. The Monte Carlo program was also used to compute the geometrical efficiency and angular resolution of the apparatus. The apparatus subtended 2π azimuthal angle. Figure 5 shows the geometrical efficiency as a function of the polar scattering angle for $\pi^\pm$ and μ^-. The efficiency for $\pi^\pm$ is smaller at small angle than that of μ^- because the scatter veto counter S was moved closer to the target to exclude as much pion decay as possible for the pion experiments. The angular-resolution correction was a 1–3% correction for the pion experiment, but was as large as 10% for the small angle part of the muon spectrum.

The multiple-scattering distribution in the target was computed using a modification of the method of Goudsmit and Saunderson.[5,6] This technique allowed the computation of a multiple-scattering distribution for any given single-scattering cross section in a given target. The ratio of multiple scattering to single scattering was computed, and the experimental data were divided by this ratio to correct for multiple scattering in the target. The ratio is relatively insensitive to the details of the single-scattering cross section for the μ^- case. For the $\pi^\pm$ case, where the exact shape of the single-scattering cross section is not initially known, it was necessary to establish the form of the multiple-scattering correction by an iteration technique. Figure 6 shows the correction ratio; the peaks for $\pi^\pm$ correspond to the filling in of the diffraction minima in the single-scattering cross section.

A correction for the finite spread of the incident momenta (spread was about 2% for μ^- and π^+, about 1% for π^-) was made on the basis of the Kisslinger model momentum dependence for the pion cross section, and on the basis of the Cou-

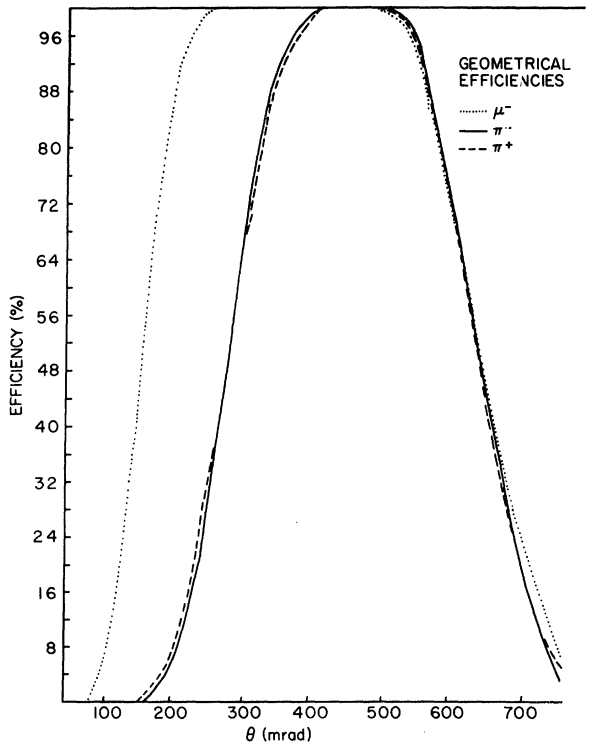

FIG. 5. Geometrical efficiencies.

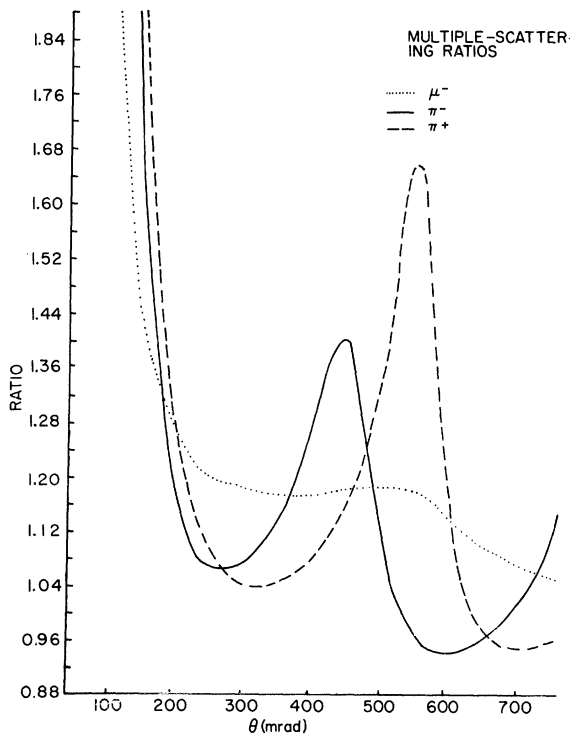

FIG. 6. Multiple-scattering ratios.

lomb scattering momentum dependence for the muons. The average pion kinetic energy was 94.9 MeV (the same for both π^+ and π^- to 0.1%), and the average muon kinetic energy was 113.0 MeV. A correction for the energy loss from the spectrometer to the target is included in these figures. The momentum-spread and energy-loss corrections together were typically 2–3% of the total elastic differential cross section, for both pions and muons.

The inclusion of the hodoscope H in the trigger, as discussed above, resulted in the need for corrections due to pion absorption and range straggling. The corrections arose because of the difference in material traversed by particles which scattered at large angles, as opposed to beam particles. The muon range was large enough so that straggling in the lead wall was negligible; but for the pion experiments, a relatively large-angle-dependent correction was necessary. A computation scheme was devised which predicted the range of an event, as measured by the system, given its momentum and scattering angle. This scheme was checked on the "beam-sample" range data which, unlike the experimental "scatter" range distribution, was not confused by large pion-decay contributions. It could correctly predict the experimentally measured pion and muon beam range spectra. The correction for pion range straggling as a function of scattering angle was then made on the basis of this scheme. The correction ranged from 2 to 30% in the 30–40° region for π^+, and from 1 to 10% in the same region for π^-. The correction for π^+ was larger, because stopped π^- produced stars via nuclear interactions, which effectively extended the range for π^-. The absorption correction was small: at most, 3%.

Although the range requirement of passage through the lead wall excluded large-energy-loss inelastic processes, inelastic events corresponding to small energy losses were still present. Our method of removal involved a calculation of the inelastic cross section which was then subtracted from the experimental data. The lead-wall requirement excluded essentially all inelastic processes in which the energy loss was greater than about 15 MeV. A calculation of the total inelastic cross section (both angular and energy loss distributions) in the single-scattering quasi-free approximation[7,8] was used as the basis of the inelastic correction.

A check on the inelastic correction was provided by an examination of the angular distribution of the events which stopped in the lead wall. This was possible for certain sections of the data, for which the hodoscope H was not required in the flux definition or trigger, but simply served to set bits in one of the data words. Selecting events for which these bits were not set was equivalent to selecting events which stopped in the lead wall. A comparison of the angular distribution of

TABLE II. Tabulation of inelastic correction for $\pi^\pm$ differential cross sections. In mb/sr, rounded to nearest whole number; uncertainties purely statistical.

	π^+			π^-		
θ(mrad)	$d\sigma/d\Omega$ Uncorrected for inelastics	Inelastic correction	$d\sigma/d\Omega$ Corrected for inelastics	$d\sigma/d\Omega$ Uncorrected for inelastics	Inelastic correction	$d\sigma/d\Omega$ Corrected for inelastics
235	6386±1614	21	6365±1614	8820±1232	40	8780±1232
265	4227±495	19	4208±495	6003±387	37	5966±387
295	2813±198	17	2796±198	3576±132	34	3542±132
325	1897±97	14	1883±97	2038±60	31	2007±60
355	1319±65	13	1306±65	1219±35	26	1193±35
385	927±51	11	916±51	636±23	23	613±23
415	657±38	9	648±38	348±16	20	328±16
445	298±27	9	289±27	178±12	19	159±12
475	213±22	10	203±22	159±11	21	138±11
505	69±16	8	61±16	163±12	18	145±12
535	35±8	6	29±8	199±13	15	184±13
565	18±6	6	12±6	230±12	13	217±12
595	18±13	4	14±13	240±13	10	230±13
625	62±18	4	58±18	215±13	8	207±13
655	71±25	3	68±25	178±15	6	172±15
685	24±36	3	21±36	129±15	6	123±15
715	103±73	2	101±73	72±19	4	68±19
740	74±126	0	74±126	29±38	3	26±38

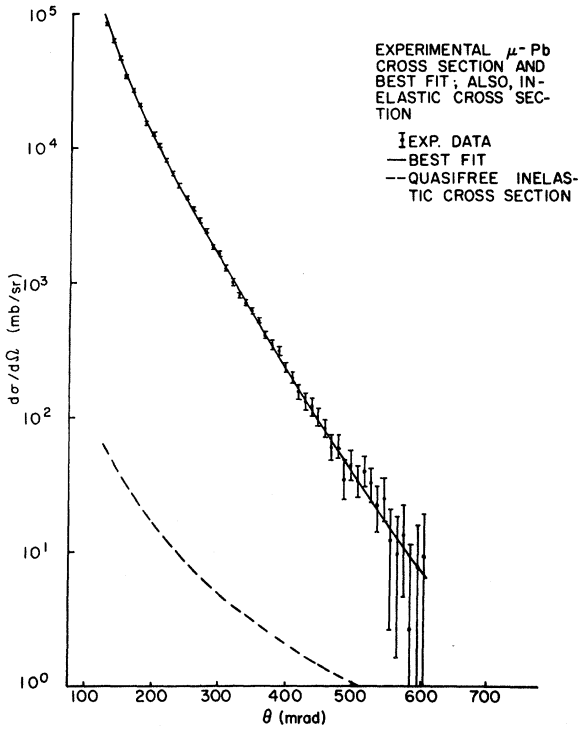

FIG. 7. Experimental μ^- Pb cross section and best fit; also, inelastic cross section.

these events with the total quasifree inelastic cross section revealed good agreement (≈20%) except at small angles (<450 mrad) where the quasifree calculation seriously underestimated the experimental distributions.

The inelastic correction to the data taken with the lead-wall requirement was made by computing the fraction of the quasifree energy-loss spectrum which would penetrate the lead wall at each angle, scaling the quasifree distribution at this angle by that fraction, and subtracting the result from the experimental data. Table II shows the experimental data before the inelastic correction, the inelastic correction, and the final result after the correction, for π^+ and π^-.

A point of concern to us was the discrepancy mentioned above between the crude experimental inelastic measurement and the quasifree calculation (at small angles). In principle, it could be possible that this discrepancy was due to the excitation of discrete low-lying levels in Pb, not correctly treated by the quasifree approximation, and so it would also be present as a contaminant even when the lead-wall requirement is imposed. However, a calculation of the excitation of some of the low-lying levels in ^{208}Pb (specifically, the 3^- state at 2.62 MeV, the 5^- state at 3.20 MeV, the 2^+ state at 4.09 MeV, and the 4^+ state at 4.32 MeV), kindly performed for us by Rost and Edwards, using a distorted-wave Born-approximation approach based on the Kisslinger model,[9] indicated that the ratio of the sum of the inelastic contribution from these levels to the elastic (in our angular range) was ~3% (i.e., consistent with the quasifree approximations). Thus, we associate the discrepancy at small angles with some process involving large energy losses, which implies that we can neglect it in the correction of the data with the lead-wall requirement present.

No inelastic corrections or radiative corrections were made to the μ^- Pb data. The inelastic contamination, calculated in the quasifree approximation, is compared to the elastic cross section in Fig. 7.

IV. RESULTS

A. Muon-Lead Experiment

The muon scattering was assumed to be entirely due to a Coulomb interaction resulting from a static charge density $\rho(r)$. The Dirac equation

TABLE III. μ^- Pb results of fits: Normalization and charge-distribution parameters fits from 125 to 695 mrad.

Charge distribution	Half-density radius [a] c(fm)	Normalization [a] N	χ^2 (55 Deg. of freedom)	$\langle r^2\rangle_{ch}^{1/2}$(fm) [b]
Fermi t =2.16 fm	6.60 ± 0.035	$1.011^{+0.005}_{-0.008}$	32.06	5.43 ± 0.035
Fermi t =2.21 fm	6.68 ± 0.058	1.012 ± 0.009	32.04	5.50 ± 0.058
Fermi t =2.26 fm	6.70 ± 0.041	1.012 ± 0.007	32.03	5.53 ± 0.041
Uniform sphere	R_c = 7.15 ± 0.05	1.018 ± 0.008	31.96	5.54 ± 0.040

[a] The errors are purely statistical. Additional errors arise from: (1) Systematic P, θ measurement errors which imply $\delta C = ^{+0.022}_{-0.036}$ fm, $\delta N = \pm 0.012$; (2) beam-sample statistics $\delta N = \pm 0.005$; (3) target contamination uncertainty $\delta N = \pm 0.005$.

[b] Assuming t = 2.21 fm (best μ–x-ray result) our final result is then

$\langle r^2\rangle_{ch}^{1/2} = 5.50^{+0.062}_{-0.068}$ fm (rms charge radius),

$N = 1.012 \pm 0.016$ (normalization).

was used to determine the scattered wave function. The solution was obtained in terms of the well-known method of partial-wave expansion. The calculations were carried out in a program written by Rawitscher[10] and kindly loaned to us for this analysis.

A Fermi shape

$$\rho(r) = \rho_0/[1 + e^{(r-c)/a}]$$

with skin thickness $t \cong 4.40a$ was chosen for the charge distribution; the data were fitted by minimizing the quantity

$$\chi^2 = \sum_i \frac{[F\sigma_{\mathrm{exp}}(\theta_i) - \sigma_{\mathrm{th}}(\theta_i)]^2}{[\delta\sigma_{\mathrm{exp}}(\theta_i)]^2},$$

allowing c [in $\rho(r)$] and F to vary. Here $\sigma_{\mathrm{exp}}(\theta_i)$ and $\delta\sigma_{\mathrm{exp}}(\theta_i)$ are the experimental cross section and its statistical uncertainty, respectively; $\sigma_{\mathrm{th}}(\theta_i)$ is the phase-shift result. The systematic uncertainties in c and F due to the uncertainties in θ and p (momentum) were also included. Additional systematic uncertainties in F arose from flux normalization statistics and the Cu contamination in the target. The results are tabulated in Table III for different assumptions about t (consistent with muonic x-ray results), and also for a uniform density

$$\rho(r) = \begin{cases} \rho_0, & r \leq R_c \\ 0, & r > R_c \end{cases}.$$

The experimental data are listed in Table IV, binned in 10-mrad bins from 125 to 695 mrad (the uncertainties are purely statistical). Figure 7 illustrates the data and the best-fit result for $t = 2.21$ fm.

B. Pion-Lead Experiments

The experimental data are listed in Table II, binned in 30-mrad bins from 235 to 740 mrad. The uncertainties are a combination of statistical and systematic pion-decay subtraction errors only. The effects of the momentum- and angle-measurement uncertainties, as well as possible normalization errors (less than 3%), have been neglected, since they do not significantly affect the optical-model comparisons discussed below.

As formulated by Auerbach and Sternheim,[3,11] the optical-model potential which describes the

TABLE IV. μ^- Pb experimental cross section (in mb/sr)(errors purely statistical).

θ (mrad)	$\frac{d\sigma}{d\Omega}$	Error	θ (mrad)	$\frac{d\sigma}{d\Omega}$	Error
125	86427	3428	415	155	18
135	62344	1956	425	131	17
145	47340	1252	435	121	17
155	33532	737	445	102	15
165	26717	539	455	84.1	14
175	20963	396	465	60.9	13
185	16332	294	475	60.4	12
195	12721	239	485	36.6	11
205	10301	191	495	46.2	11
215	8121	158	505	34.8	10
225	6554	141	515	40.9	10
235	5292	122	525	33.7	10
245	4282	106	535	22.8	9
255	3534	94	545	26.6	9
265	2978	85	555	11.6	9
275	2460	78	565	9.8	8.4
285	1828	66	575	13.7	9.1
295	1660	61	585	2.7	8.7
305	1296	55	595	6.4	9.5
315	990	48	605	9.4	10.3
325	811	44	615	8.1	10.9
335	705	39	625	10.0	11.8
345	619	36	635	4.0	12.6
355	525	33	645	4.5	14.0
365	412	29	655	7.9	15.0
375	346	28	665	1.5	17.6
385	311	25	675	6.0	20.1
395	236	22	685	8.6	22.3
405	195	21	695	6.7	30.0

elastic scattering of a pion by a nucleus (Z,A) is

$$\nu^{\pi^\pm}(\vec{r}) = (-A/2E_\pi)\{(Z/A)[k^2 b_0^{(\pi^\pm p)} - b_1^{(\pi^\pm p)}\vec{\nabla}(\rho_p(r)\vec{\nabla})] + (A-Z)/A[k^2 b_0^{(\pi^\pm n)}\rho_n(r) - b_1^{(\pi^\pm n)}\vec{\nabla}(\rho_n(r)\vec{\nabla})]\}\,. \quad (1)$$

Here k is the incident pion momentum, E_π the incident pion total energy, and b_0, b_1 are parameters related to the s- and p-wave parts of the pion-nucleon interaction, averaged over the Fermi momentum distribution of the nucleus. In using the optical potential above to generate a cross section, a Coulomb potential corresponding to a uniformly charged sphere of radius $R_c = 7.035$ fm was included in a modified Klein-Gordon equation which was solved by a partial-wave analysis, in a program (ABACUSM)[12] written by Auerbach and Sternheim and kindly loaned to us for this analysis. Details are discussed in Ref. 3. Assuming charge independence, we have $b_l^{(\pi^\pm p)} = b_l^{(\pi^- n)}$ and $b_l^{(\pi^+ n)} = b_l^{(\pi^- p)}$, $l = 0, 1$.

The nucleon densities ρ_p, ρ_n are Fermi shapes (p = proton, n = neutron):

$$\rho_{p,n}(r) = \frac{\rho_0}{1+\exp[(r-c_{p,n})/a_{p,n}]}\,,$$

$$\int \rho_{p,n}(r)d^3r = 1\,.$$

In the initial comparisons, we have chosen $\rho_p = \rho_n$, with $c_p = c_n = 6.67$ fm, $a_p = a_n = 0.5$ fm (the values corresponding to the Fermi-shape charge density).

Then we may define the average parameters for $l = 0, 1$:

$$\bar{b}_l^{\pi^+} \equiv \left(\frac{1}{A}\right)[Zb_l^{(\pi^+ p)} + (A-Z)b_l^{(\pi^+ n)}]\,,$$
$$\bar{b}_l^{\pi^-} \equiv \left(\frac{1}{A}\right)[Zb_l^{(\pi^+ n)} + (A-Z)b_l^{(\pi^+ p)}]\,; \quad (2)$$

and the optical potential simplifies to

$$\nu^{\pi^\pm}(\vec{r}) = (-A/2E_\pi)[k^2\bar{b}_0^{\pi^\pm}\rho(r) - \bar{b}_1^{\pi^\pm}\vec{\nabla}(\rho(r)\vec{\nabla})]\,,$$

where $\rho(r) = \rho_p(r) = \rho_n(r)$.

The first comparisons of the data with the optical model were made to find the best-fit optical parameter $\bar{b}_l^{\pi^\pm}$. (The approximations made in the theory make it necessary to allow for changes in the $\bar{b}_l^{\pi^\pm}$ parameters from their theoretical values.) We compute the quantity

$$\chi^2_{\pi^\pm} = \frac{1}{N}\sum_{i=1}^{N}\frac{[\sigma^{\pi^\pm}_{\rm exp}(\theta_i) - \sigma^{\pi^\pm}_{\rm th}(\theta_i)]^2}{[\delta\sigma^{\pi^\pm}_{\rm exp}(\theta_i)]^2}\,.$$

$\sigma^{\pi^\pm}_{\rm exp}(\theta_i)$ and $\delta\sigma^{\pi^\pm}_{\rm exp}(\theta_i)$ are, respectively, the experimental cross section and its uncertainty, as listed in Table II. $\sigma^{\pi^\pm}_{\rm th}(\theta)$ is the cross section computed

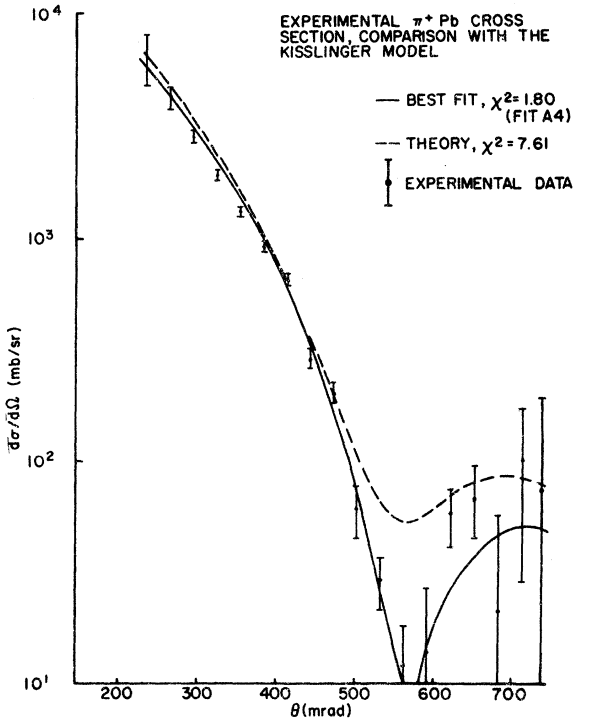

FIG. 8. Experimental π^+ Pb cross section, comparison with the Kisslinger model.

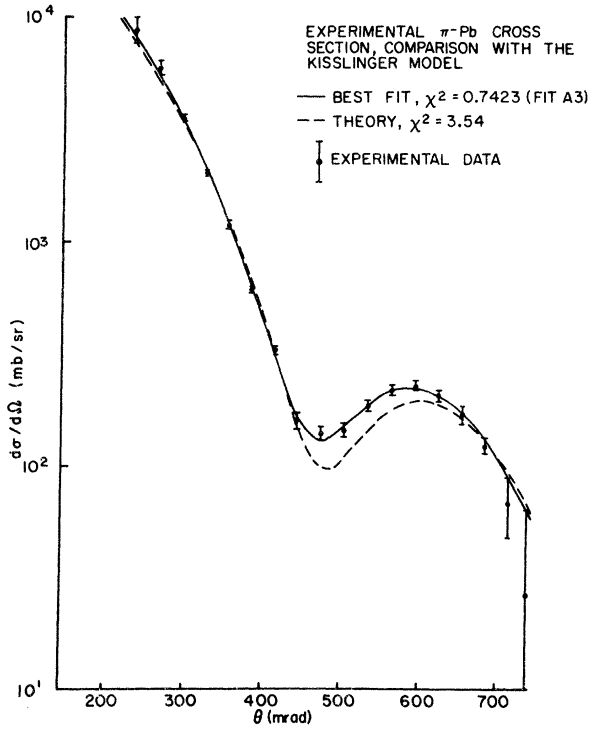

FIG. 9. Experimental π^- Pb cross section, comparison with the Kisslinger model.

from the optical model. Starting with the $\bar{b}_l^{\pi^\pm}$ values computed from Fermi averaged experimental pion-nucleon phase shifts (as given in Ref. 11), we vary $\bar{b}_l^{\pi^\pm}$ to minimize $\chi^2{}_{\pi^\pm}$. The $\bar{b}_l^{\pi^\pm}$ values which minimize $\chi^2{}_{\pi^\pm}$ are not unique; we have chosen the combination which both produces a good fit and is least distant from the theoretical values.

Figures 8 and 9 illustrate the data and the optical-model predictions for the theoretical $\bar{b}_l^{\pi^\pm}$ values, and the best-fit $\bar{b}_l^{\pi^\pm}$ values. The best-fit results give an excellent fit. Attempts to fit the data using the simple optical model (no p-wave dependence, $b_1 = 0$, only b_0 varied) cannot produce good fits. Table V lists the optical-model parameters, both best-fit and theoretical values. In addition, the more basic $b_l^{(\pi^+ p)}$, $b_l^{(\pi^+ n)}$ parameters are listed; the "fit" values are obtained by solving Eqs. (2) for $b_l^{(\pi^+ p)}$, $b_l^{(\pi^+ n)}$, using the best-fit $\bar{b}_l^{\pi^\pm}$ on the left-hand side.

The neutron-density dependence of the data was studied first by examining the π^+ and π^- distributions independently. It is probably not necessary (and is, in any case, quite difficult) to vary all the optical parameters and density distribution parameters to obtain a good fit. Therefore, we have fixed $b_0^{(\pi^+ p)}$, $b_0^{(\pi^+ n)}$, and the p-wave strength parameter corresponding to the protons (i.e., $b_1^{(\pi^+ p)}$ for π^+ and $b_1^{(\pi^+ n)}$ for π^-) at their best-fit values as found for $\rho_p = \rho_n$ above; we have also fixed ρ_p equal to the normalized charge density, as above. We allow the neutron strength parameter ($b_1^{(\pi^+ n)}$ for π^+, $b_1^{(\pi^+ p)}$ for π^-) to vary (both real and imaginary parts) along with the neutron density parameters c_n, a_n in search of a minimum $\chi^2{}_{\pi^\pm}$. We find a considerable (correlated) variation in $\mathrm{Re}b_1$ and c_n, and in $\mathrm{Im}b_1$ and a_n, which allows equally good fits to the data. This makes the determination of neutron density parameters considerably less accurate and more complicated than would otherwise be the case. The results of extensive scans of the parameter spaces indicate the following neutron-matter rms radius determinations.

For π^- only,

$$\langle r^2\rangle^{1/2} = 5.50^{+0.15}_{-0.40} \text{ fm for } 0.4 \leq a_n \leq 0.6 \text{ fm},$$

$$\langle r^2\rangle^{1/2} = 5.58 \pm 0.10 \text{ fm for } a_n = 0.5 \text{ fm}.$$

TABLE V. $\pi^\pm$ Pb results of fits: Optical-model parameters and neutron-matter distribution parameters. Fits from 235 to 740 mrad. b_l in fm^3.

1. Assuming equal proton-neutron densities

Parameter	Theory	χ^2	Best fit	χ^2
A. Simple optical model, averaged parameters				
$b_0^{\pi^-}$	$8.42 + i6.48$	15.68	$8.46 + i3.86$	8.15
$b_0^{\pi^+}$	$7.33 + i5.38$	15.01	$7.19 + i3.36$	9.31
B. Kisslinger model, averaged parameters				
$b_0^{\pi^-}$	$-1.42 + i\,0.47$	3.54	$-1.42 + i0.47$	0.742
$b_1^{\pi^-}$	$9.84 + i\,6.01$		$12.29 + i3.51$	
$b_0^{\pi^+}$	$-0.51 + i\,0.46$	7.62	$-3.5 + i0.46$	1.80
$b_1^{\pi^+}$	$7.84 + i4.92$		$8.5 + i1.5$	
C. Kisslinger model, basic parameters				
$b_0^{(\pi^+ p)}$	$-3.12 + i0.48$		$2.46 + i0.48$	
$b_0^{(\pi^+ n)}$	$1.18 + i0.45$		$-7.34 + i0.44$	
$b_1^{(\pi^+ p)}$	$13.55 + i8.05$		$19.35 + i7.25$	
$b_1^{(\pi^+ n)}$	$4.13 + i2.88$		$1.44 + i(-2.24)$	

2. Assume $a_n = 0.5$ fm, fix $b_0^{(\pi^+ p)}$, $b_0^{(\pi^+ n)}$ as specified in "best-fit" table in 1C above

   A. Fit π^- only, fix $b_1^{(\pi^+ n)}$ = "best-fit" value, vary c_n and $b_1^{(\pi^+ p)}$
   Result: Minimum χ^2 (0.69) at $c_n = 6.79$ fm, $\langle r^2\rangle_n{}^{1/2} = 5.58$ fm, $b_1^{(\pi^+ p)} = 16.0 + 8.0i$

   B. Fit π^+ only, fix $b_1^{(\pi^+ p)}$ = "best-fit" value in 1C above, vary c_n and $b_1^{(\pi^+ n)}$
   Result: Minimum χ^2 (1.37) at $c_n = 6.27$ fm, $\langle r^2\rangle_n{}^{1/2} = 5.20$ fm, $b_1^{(\pi^+ n)} = -2.5. + i\,(-4.0)$

   C. Fit $\pi^\pm$ together (using D, A quantities), fix $\mathrm{Im}\,b_1^{(\pi^+ n)}$, $\mathrm{Im}\,b_1^{(\pi^+ p)}$ = "best-fit" values in 1C above, vary c_n and $\mathrm{Re}\,b_1^{(\pi^+ p)}$, $\mathrm{Re}\,b_1^{(\pi^+ n)}$
   Result: Best fit at $\mathrm{Re}\,b_1^{(\pi^+ n)} = 0.0$, $\mathrm{Re}\,b_1^{(\pi^+ p)} = 22.0$, $c_n = 6.63$ fm, $\langle r^2\rangle_n{}^{1/2} = 5.45$ fm, $\chi^2{}_{\pi^-} = 0.80$, $\chi^2{}_{\pi^+} = 1.85$

For π^+ only,

$$\langle r^2\rangle^{1/2} = 5.52^{+0.10}_{-0.20} \text{ fm for } 0.4 \leq a_n \leq 0.6 \text{ fm},$$

$$\langle r^2\rangle^{1/2} = 5.20 \pm 0.10 \text{ fm for } a_n = 0.5 \text{ fm}.$$

It is clear that the results are inconsistent for the assumption $a_n = 0.5$ fm. In addition, we emphasize that the fits which produce the above numbers are obtained by varying some of the optical parameters, so that, as shown in Table V, they are not the same for π^+ and π^-. However, by constructing the quantities

$$A(\theta) = \sigma_{\pi^+}(\theta) + \sigma_{\pi^-}(\theta)$$

and

$$D(\theta) = [\sigma_{\pi^-}(\theta) - \sigma_{\pi^+}(\theta)]/A(\theta)$$

and fitting to a weighted combination, we can find the best-fit optical parameters and neutron density for a properly weighted combination of π^+ and π^- data. The fitting was done by varying c_n, along with $\mathrm{Re}b_1^{(\pi^+p)}$ and $\mathrm{Re}b_1^{(\pi^+n)}$, with $a_n = 0.5$ fm and the other optical parameters at their best-fit values found for $\rho_p = \rho_n$ above. We have not varied the imaginary parts of the parameters or a_n, in the interests of simplicity. The result was

$$\langle r^2\rangle^{1/2} = 5.45^{+0.10}_{-0.04} \text{ fm}, \quad a_n = 0.5 \text{ fm}.$$

The best-fit optical parameters are indicated in Table V.

Another less direct but probably more model-independent method of extracting relative neutron-proton rms radius information involves a comparison of the total nuclear size as seen by π^- vs that seen by π^+. Since π^- is more sensitive to neutrons than protons and vice versa for π^+ (because of the relative dominance of the p-wave triplet isospin state phase shift), a larger apparent nuclear size for π^- than for π^+ would indicate that the neutron distribution rms radius was larger than that of the protons. Shifts in the actual absolute radius values which the theoretical uncertainties might introduce (as they introduced changes in the b_l parameters) would not bias this comparison, provided they are the same for π^+ and π^-. Unfortunately, although the total nuclear rms radius (assuming $\rho_p = \rho_n$) is well defined for π^-, this is not the case for π^+: Our data only determine the total nuclear rms radius for π^+ to $\sim\pm 1$ fm, when we allow the proton distribution to vary, because increases in the proton rms radius can be partially compensated by increases in the neutron rms radius. Thus, although this method is sound in principle, in our case the nuclear size is not well enough determined for π^+ to allow it application as a check on our other techniques.

V. CONCLUSION

The interpretation of the preceding results for the muon-lead cross section is rather straightforward. A simple calculation based on the Dirac equation and a static charge density produces excellent agreement with the data. The rms radius is seen to be the same (within our statistical error) for a uniform sphere model and the more usual Fermi shape. The rms radius (5.50 ± 0.06 fm) compares well with both the results of muonic x-ray studies[13] (5.493 ± 0.007 fm) and electron scattering[13] (5.50 ± 0.06 fm). The normalization agrees with that predicted by the Dirac equation. The pion data are fitted surprisingly well by the Kisslinger model (especially the π^- data), considering the crudeness of some of the approximations made. The failure of the simple optical model once again verifies the superiority of the Kisslinger model.

The variations in $\bar{b}_l^{\pi^\pm}$ needed to fit the $\pi^\pm$ data (for the assumption of equal normalized nucleon and charge densities) are typical of the variations found by others[3, 14, 15] in fitting to the Kisslinger model. It is interesting that the best-fit optical parameter b_1 for π^- ($\bar{b}_1^{\pi^-} = 12.29 + i\,3.51$) is related to the theoretical value ($\bar{b}_1^{\pi^-} = 9.84 + i\,6.01$) in much the same way that the best-fit parameter found by Auerbach and Sternheim[14] for the π^--^{12}C (CERN) data at $T_\pi = 120$ MeV ($\bar{b}_1^{\pi^-} = 9.24 + i\,3.14$) is related to the theoretical value in that case ($\bar{b}_1^{\pi^-} = 7.34 + i\,7.15$). This implies a relative A independence of the shifts of the best-fit parameters from the theoretical values and suggests examinations of pion scattering in nuclei of intermediate A to see if the pattern persists.

The differences between the $b_l^{(\pi^+p)}$, $b_l^{(\pi^+n)}$ parameters resulting from the fits, and the theoretical values, are seen to be quite large in some cases. They are hard to reconcile with the relatively mild changes found for the averaged parameters $\bar{b}_l^{\pi^\pm}$. It is possible that these large deviations may be more a reflection of an inconsistency between the independent $\pi^\pm$ fits [due, for example, to neglected charge-dependent effects in $\nu^{\pi^\pm}(r)$] than an indication of changes caused by the approximations made in the optical potential derivation. In this connection, we note that Marshall *et al.*[15] in the only recent $\pi^\pm$ comparison (for ^{12}C and ^{16}O at 30 MeV) concluded that they could not find consistent optical parameters for both π^+ and π^-. They noted that further refinements in the theory might resolve the difficulty. Whatever the cause of the problem with the $b_l^{(\pi^+p)}$, $b_l^{(\pi^+n)}$ parameters, we can certainly say that the Kisslinger model provides an excellent semiphenomenological description of the elastic scattering of $\pi^\pm$ from Pb

at $T_\pi \sim 100$ MeV up to angles of about 40°.

The neutron density rms radius determination unfortunately also has some inconsistencies. The rms radii found for π^+ and π^-, under assumption $a_n = 0.5$ fm, are inconsistent. This inconsistency probably indicates the level at which the reliability of the theory enters into the radius determination. It would suggest that the best estimate of the uncertainty associated with the most consistent result (the D, A fit of 5.45 fm) should be determined by the difference between the independent π^+ and π^- fit results. We therefore conclude that the best radius determination, for the assumption $a_n = 0.5$ fm, is

$$\langle r^2 \rangle^{1/2} = 5.45^{+0.13}_{-0.25} \text{ fm}.$$

The independent π^+ and π^- fit results indicate that relaxing the assumption $a_n = 0.5$ fm will probably not change this result significantly.

Taking the muonic x-ray value for $\langle r^2 \rangle_{\text{ch}}^{1/2}$ (5.49 fm),[13] then the neutron-proton rms radius difference is

$$\delta_{pn} = -0.04^{+0.13}_{-0.25} \text{ fm} \quad \text{if } a_n = 0.5 \text{ fm}.$$

This result is in agreement with the neutron radius as determined from $\pi^\pm$ absorption cross sections,[16] but is somewhat smaller than the radius derived from recent α-scattering[17] and sub-Coulomb pick-up[18] experiments (see Fig. 1). An improvement in the neutron radius determination by pion-scattering techniques would require elastic differential cross-section measurements at larger angles and more energies.[4] The correlated excursions in optical parameters and neutron density parameters, which contribute to the uncertainty in this measurement, should then be diminished. In addition, of course, the possible $\pi^\pm$ inconsistencies found here should be resolved (possibly by a more sophisticated theoretical analysis), if the theory is to be trusted to the extent that reliable nuclear-structure information can be obtained.

ACKNOWLEDGMENTS

We would like to acknowledge the assistance of the Nevis Laboratory staff members who contributed to the performance of this experiment. Thanks are also due to the V. W. Hughes's Group at Yale for their loan of the magnetostrictive-readout wire spark chambers. We would like to thank Dr. E. Rost and Dr. G. Edwards at the University of Colorado for their calculation of inelastic cross sections; also, Professor G. Rawitscher of Yale for the loan of the computer program YALEROF, which was used to compute the muon-lead cross section. We must especially thank Professor M. M. Sternheim at the University of Massachusetts for the use of the program ABACUSM, which was used to compute the pion-lead cross sections in the Kisslinger model. Finally, the helpful suggestions of Professor James Rainwater concerning the analysis are also acknowledged.

---

*Research supported in part by the National Science Foundation.

†Present address: Rutherford High Energy Laboratory, Didcot, Chilton, Berkshire, England.

[1]F. Binon *et al.*, Nucl. Phys. B17, 168 (1970).
[2]L. S. Kisslinger, Phys. Rev. 98, 761 (1956).
[3]E. H. Auerbach *et al.*, Phys. Rev. 162, 1683 (1967).
[4]L. S. Kisslinger *et al.*, Phys. Rev. C 6, 469 (1972).
[5]S. Goudsmit and J. L. Saunderson, Phys. Rev. 57, 24 (1940).
[6]S. Goudsmit and J. L. Saunderson, Phys. Rev. 58, 36 (1940).
[7]T. K. Fowler and K. M. Watson, Nucl. Phys. 13, 549 (1959).
[8]M. H. Johnson, Phys. Rev. 83, 510 (1951).
[9]G. W. Edwards and E. Rost, Phys. Rev. Lett. 26, 785 (1971).
[10]G. Rawitscher, Phys. Rev. 112, 1274 (1958).
[11]E. H. Auerbach and M. M. Sternheim, Phys. Rev. C 4, 1805 (1971).
[12]E. H. Auerbach and M. M. Sternheim, BNL Report No. 12096 (unpublished).
[13]J. Wilets and C. S. Wu, Annu. Rev. Nucl. Sci. 19, 527 (1969).
[14]E. H. Auerbach and M. M. Sternheim, Phys. Rev. Lett. 25, 1500 (1970).
[15]J. F. Marshall *et al.*, Phys. Rev. C 1, 1685 (1970).
[16]E. H. Auerbach *et al.*, Phys. Rev. Lett. 21, 162 (1968).
[17]A. M. Bernstein and W. A. Seidler, unpublished.
[18]H. J. Korney and J. P. Schiffer, Phys. Rev. Lett. 27, 1457 (1971).